Letter

Tailored Ising superconductivity in intercalated bulk NbSe$_2$

Haoxiong Zhang[1], Awabaikeli Rousuli[1], Kenan Zhang[1], Laipeng Luo[1], Chenguang Guo[1], Xin Cong[2], Zuzhang Lin[1], Changhua Bao[1], Hongyun Zhang [1], Shengnan Xu[1], Runfa Feng[1], Shengchun Shen[1], Kun Zhao[1], Wei Yao [1], Yang Wu[3], Shuaihua Ji[1,4], Xi Chen [1,4], Pingheng Tan [2], Qi-Kun Xue[1,4], Yong Xu [1,4], Wenhui Duan [1,4], Pu Yu [1,4] and Shuyun Zhou[1,4] ✉

Reducing the dimensionality of layered materials can result in properties distinct from their bulk crystals[1–3]. However, the emergent properties in atomically thin samples, in particular in metallic monolayer flakes, are often obtained at the expense of other important properties. For example, while Ising superconductivity—where the pairing of electrons with opposite out-of-plane spins from K and K′ valleys leads to an in-plane upper critical field exceeding the Pauli limit—does not occur in bulk NbSe$_2$, it was observed in two-dimensional monolayer flakes[4]. However, the critical temperature was reduced as compared to bulk crystals[4–13]. Here we take a different route to control the superconducting properties of NbSe$_2$ by intercalating bulk crystals with cations from ionic liquids. This produces Ising superconductivity with a similar critical temperature to the non-intercalated bulk and is more stable than in a monolayer flake. Our angle-resolved photoemission spectroscopy measurements reveal the effectively two-dimensional electronic structure, and a comparison of the experimental electronic structures between intercalated bulk NbSe$_2$ and monolayer NbSe$_2$ film reveals that the intercalant induces electron doping. This suggests ionic liquid cation intercalation is an effective technique for controlling both the dimensionality and the carrier concentration, allowing tailored properties exceeding both bulk crystals and monolayer samples.

In monolayer niobium diselenide (NbSe$_2$), the non-centrosymmetric crystalline structure together with the spin–orbit interaction locks the spin to the out-of-plane direction, resulting in Ising superconductivity[4] with an exceedingly high upper critical field of up to 31.5 T. Such Ising superconductivity is intriguing; however, the superconducting critical temperature T_c is reduced from 7.0 K in the bulk crystal to 0.9–3.7 K (below the liquid helium temperature) in monolayer samples[4,7–13], and the monolayer metallic sample is unstable at ambient environment[4,11]. The reduction of T_c with thickness is surprising, since the observation of superconducting gap in the two-dimensional (2D) Nb $4d$ derived bands but not in the three-dimensional (3D) Se p_z derived bands[14,15] suggests that the superconductivity is mainly contributed by the 2D Nb $4d$ bands. While different scenarios including enhanced Coulomb interaction or thermal fluctuations in two dimensions[4,7], changes in the band structure[8,9] and competition between superconductivity and

[1]State Key Laboratory of Low-Dimensional Quantum Physics and Department of Physics, Tsinghua University, Beijing, China. [2]State Key Laboratory of Superlattices and Microstructures, Institute of Semiconductors, Chinese Academy of Sciences, Beijing, China. [3]Department of Mechanical Engineering and Tsinghua-Foxconn Nanotechnology Research Center, Tsinghua University, Beijing, China. [4]Frontier Science Center for Quantum Information, Beijing, China. ✉e-mail: syzhou@mail.tsinghua.edu.cn
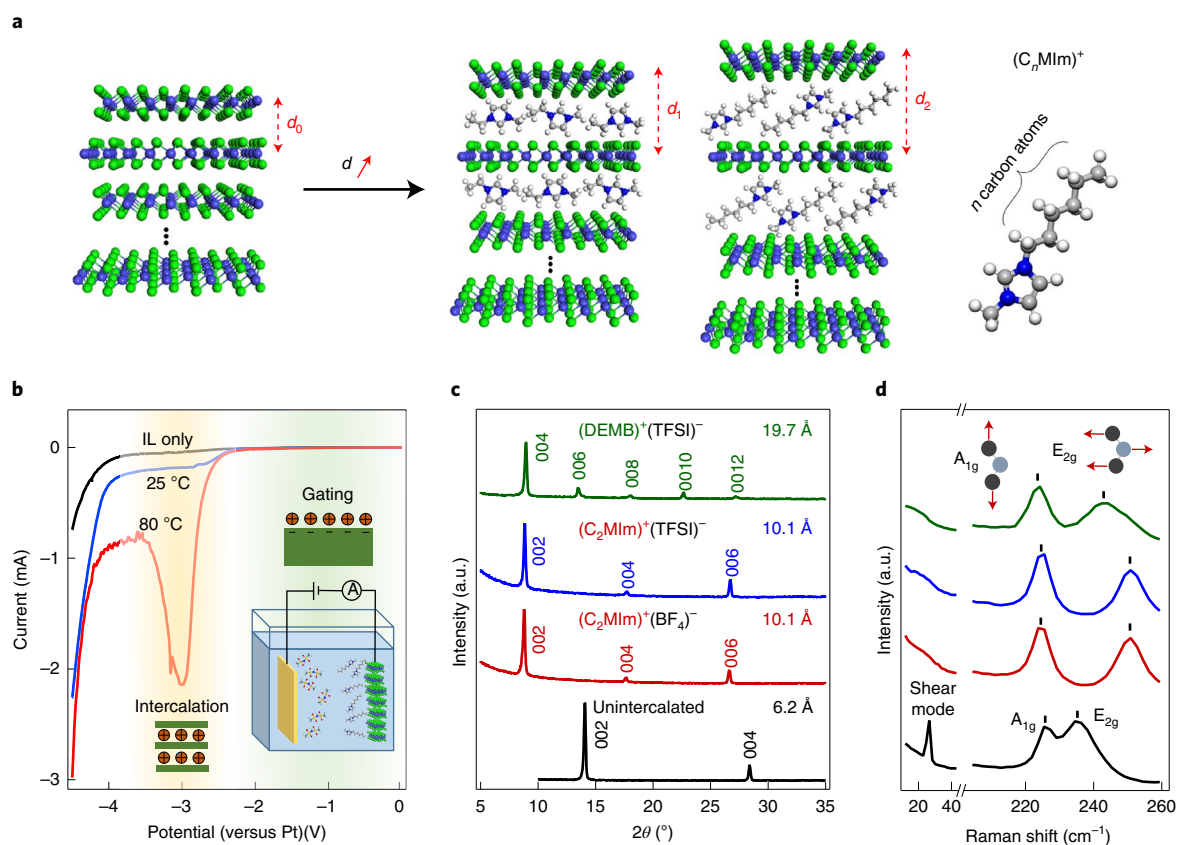
Fig. 1 | Schematic for tuning the interlayer interaction via ionic intercalation and evidence for successful intercalation of organic cations into $NbSe_2$ crystal. a, Schematic drawing for tuning the interlayer spacing (d) through ionic intercalation. The right panel is a schematic drawing for intercalated imidazole cations [C_nMIm]$^+$ (1-alkyl-3-methylimidazolium), where n represents the length of the alkane carbon chain. The green, purple, blue, grey and white atoms represent Se, Nb, N, C and H, respectively. **b**, Current–voltage (I–V) curves with IL only (black curve) and IL with $NbSe_2$ sample at two different temperatures (blue and red curves). A schematic drawing for the experimental set-up is shown in the inset. The green shared region corresponds to the gating region, while intercalation occurs in the orange shaded region. **c**, XRD data of three intercalated samples with different ILs compared with the unintercalated bulk sample. The error bar for the lattice constant is ±0.1 Å. [TFSI]$^-$ (bis(trifluoromethylsulfonyl)imide) is a commonly IL anion used, and [BF_4]$^{-1}$ (tetrafluoroborate) is used for comparison. **d**, Raman spectra of intercalated samples with three ILs compared with the unintercalated bulk sample. The vibrational modes of A_{1g} and E_{2g} are shown on the top of this panel.

charge density wave (CDW)[16–18] have been proposed, the origin remains elusive.

Instead of reducing the sample thickness, which is widely used to control the dimensionalities of layered materials, an emerging attractive strategy for controlling the interlayer interaction is to expand the interlayer spacing by intercalating ions with large size into the van der Waals gap of the layered crystals, as schematically illustrated in Fig. 1a. Such intercalation provides a convenient pathway for band structure engineering, namely, maintaining the 2D bands while reducing or removing the contribution of 3D bands. Moreover, the intercalated ions can also inject carriers into the bulk crystal, thereby achieving simultaneous control of the dimensionality and carrier concentration. Developing a convenient experimental pathway for ionic intercalation and experimentally evaluating its tunability are both highly desirable. In this Article, using $NbSe_2$ as a model layered crystal and [C_2MIm]$^+$ (1-ethyl-3-methylimidazolium with the chemical formula of [$C_6H_{11}N_2$]$^+$; see Supplementary Fig. 1 for the structure and size) as an example for organic ions, we demonstrate the successful intercalation of cations from ionic liquids (ILs) into the van der Waals gap of the layered crystal, resulting in Ising superconductivity with a T_c = 6.9 K higher than any monolayer $NbSe_2$ flake or film reported so far[4,7–13]. Angle-resolved photoemission spectroscopy (ARPES) measurements reveal the role of the intercalated cations in reducing the dimensionality and tuning the carrier concentration.

Although ILs have been widely used for tuning the charge carrier concentration[19–24], their application as intercalants for layered crystals has been discovered only recently in Weyl semimetals $MoTe_2$ and WTe_2(ref. [25]) and semiconducting $SnSe_2$(ref. [26]), leading to enhanced or induced superconductivity in the intercalated organic–inorganic hybrid crystals. Here we apply this method to $NbSe_2$, where highly improved sample quality can be obtained after optimizing the intercalation conditions, allowing to reveal not only the intriguing phenomena but also the underlying physics from ARPES measurements. Figure 1b shows a schematic drawing of the intercalation process, and the experimental set-up is shown in Supplementary Fig. 2. At low voltages (green shaded region in Fig. 1b), electrons are injected into the interface between $NbSe_2$ and the ionic liquid similar to previous electrostatic gating experiments[19–24], while at a higher voltage and a higher temperature, the electrochemical intercalation becomes favourable (orange shaded region in Fig. 1b). The intercalation process typically starts from the surfaces and the edges of the single-crystal sample (Supplementary Fig. 3), and the full intercalation of a bulk single crystal with a typical thickness of 100 μm can be completed within a few hours using the optimum intercalation conditions in Supplementary Table 1.

The successful intercalation of IL cations into the crystal is confirmed by X-ray diffraction (XRD) and Raman spectroscopy measurements shown in Fig. 1c,d, respectively. After the intercalation, the diffraction peaks from the bulk $NbSe_2$ with an interlayer spacing of
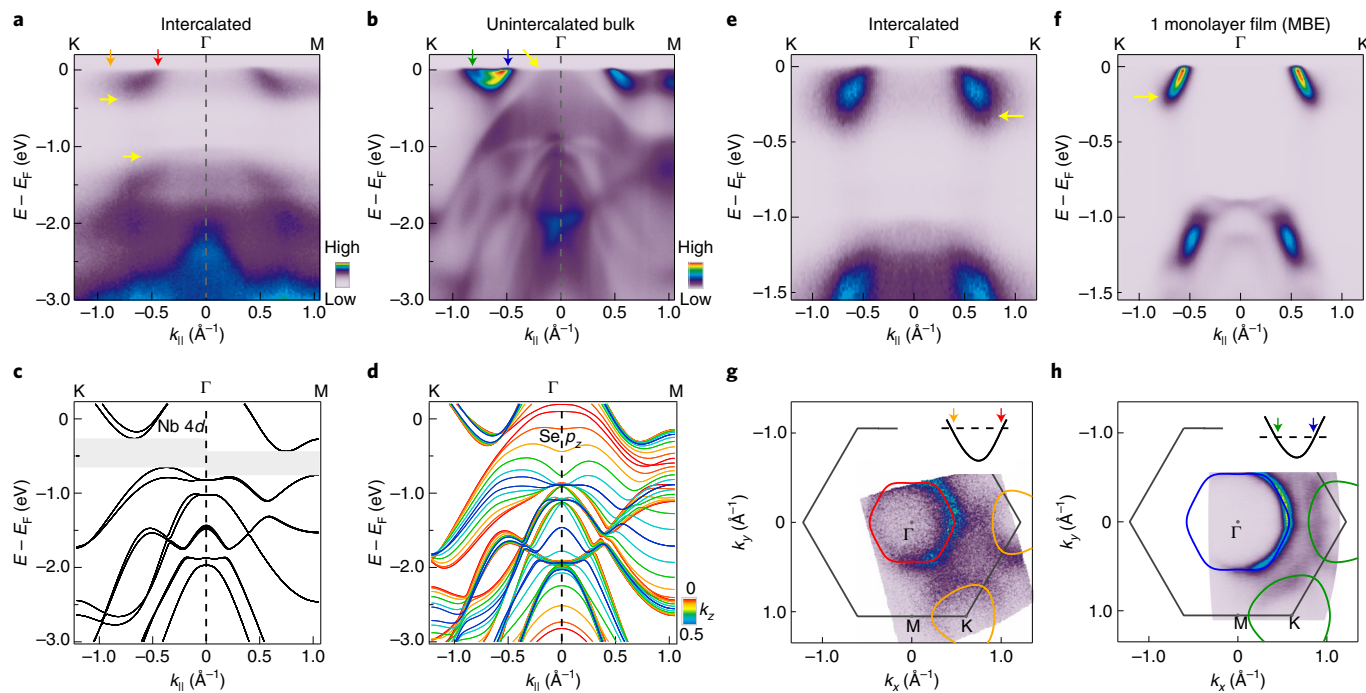
Fig. 2 | Electronic structure of intercalated NbSe₂ compared with uninteralated bulk sample and monolayer film, showing layer-decoupled electronic structure and electron doping for the intercalated sample. **a,b**, Comparison of dispersions along the K–Γ–M direction for intercalated (**a**) and uninteralated bulk (**b**) NbSe₂ samples. The ARPES intensity is indicated by a linear colour scale, as indicated by the colour bar. **c,d**, Calculated dispersion of

NbSe₂ with interlayer spacing of 9.9 Å (**c**) and 6.2 Å (**d**) along the K–Γ–M direction. $k_z = 0$ is shown in **c** and varying k_z is shown in **d**, corresponding to monolayer and bulk samples, respectively. The colour scale indicates the variation of calculated k_z from 0 to 0.5. **e,f**, Comparison of zoom-in dispersions along the K–Γ–K direction for intercalated NbSe₂ (**e**) and monolayer MBE film (**f**). **g,h**, Fermi surface maps for intercalated NbSe₂ (**g**) and monolayer MBE film (**h**).
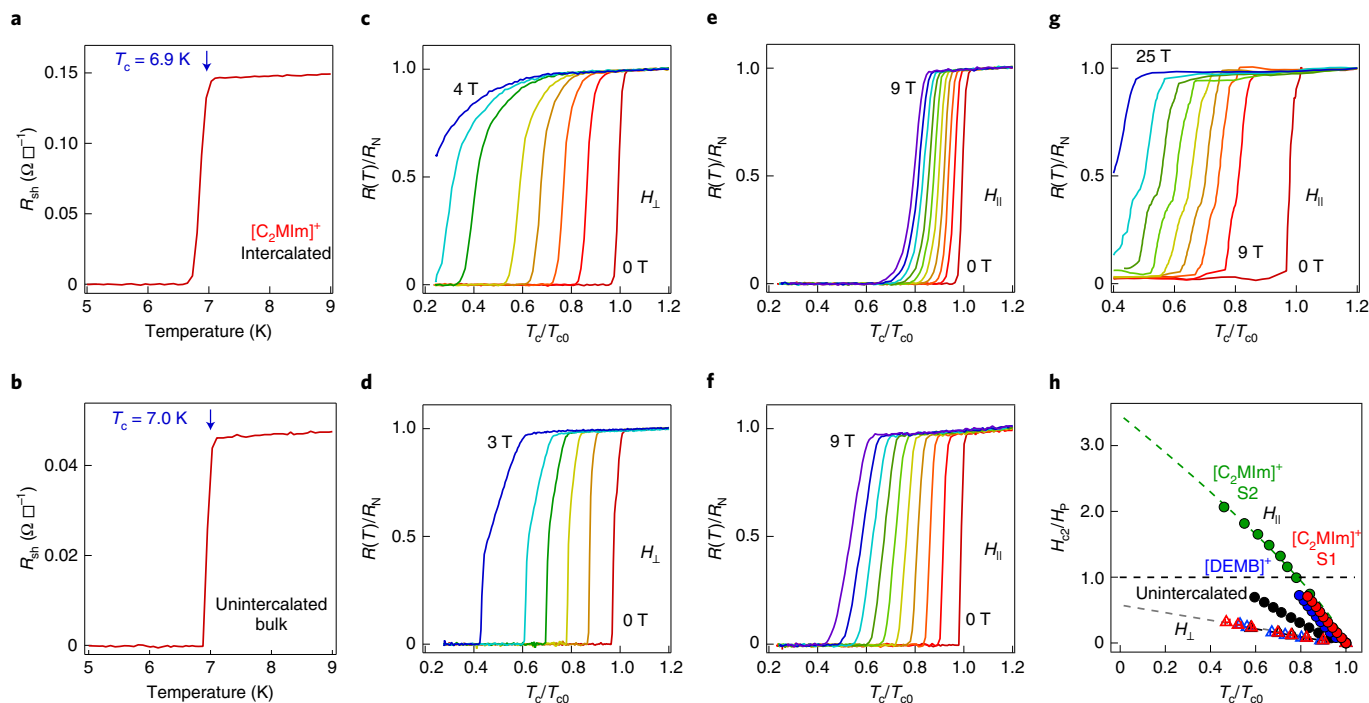

Fig. 3 | Tailored Ising superconductivity in the intercalated sample. **a,b**, Comparison of temperature-dependent sheet resistance of [C₂MIm]⁺-intercalated (**a**) and [C₂MIm]⁺-uninteralated bulk (**b**) samples. **c–g**, Resistance under different out-of-plane magnetic fields ($H_\perp$) and in-plane magnetic fields ($H_\parallel$) for [C₂MIm]⁺-intercalated (**c,e,g**) and [C₂MIm]⁺-uninteralated (**d,f**) bulk samples. The out-of-plane magnetic fields are 0, 0.5, 1, 1.5, 2, 3, 3.5 and 4 T from the red to the blue curves in **c** and 0, 0.5, 1, 1.5, 2 and 3 T from the red to the blue curves in **d**. The in-plane magnetic fields are 0, 1, 2, 3, 4, 5, 6, 7, 8 and 9 T from the

red to the purple curves in **e** and **f** and 0, 9, 12, 14, 16, 18, 20, 22 and 25 T from the red to the blue curves in **g**. The data were normalized by the resistance at 8 K (above T_c). **h**, Extracted upper critical magnetic fields H_{c2} for $H_\perp$ and $H_\parallel$ as a function of temperature. The grey dashed curve is fitted by 2D Ginzburg–Landau equation, and the green dashed curve is fitted using $H_{c2,\parallel}(T) = H_{c2,\parallel}^*(1 - T/T_c)^{1+x}$. H_P is the Bardeen–Cooper–Schrieffer Pauli paramagnetic limit. The error bar from the fitting is smaller than the symbol size.
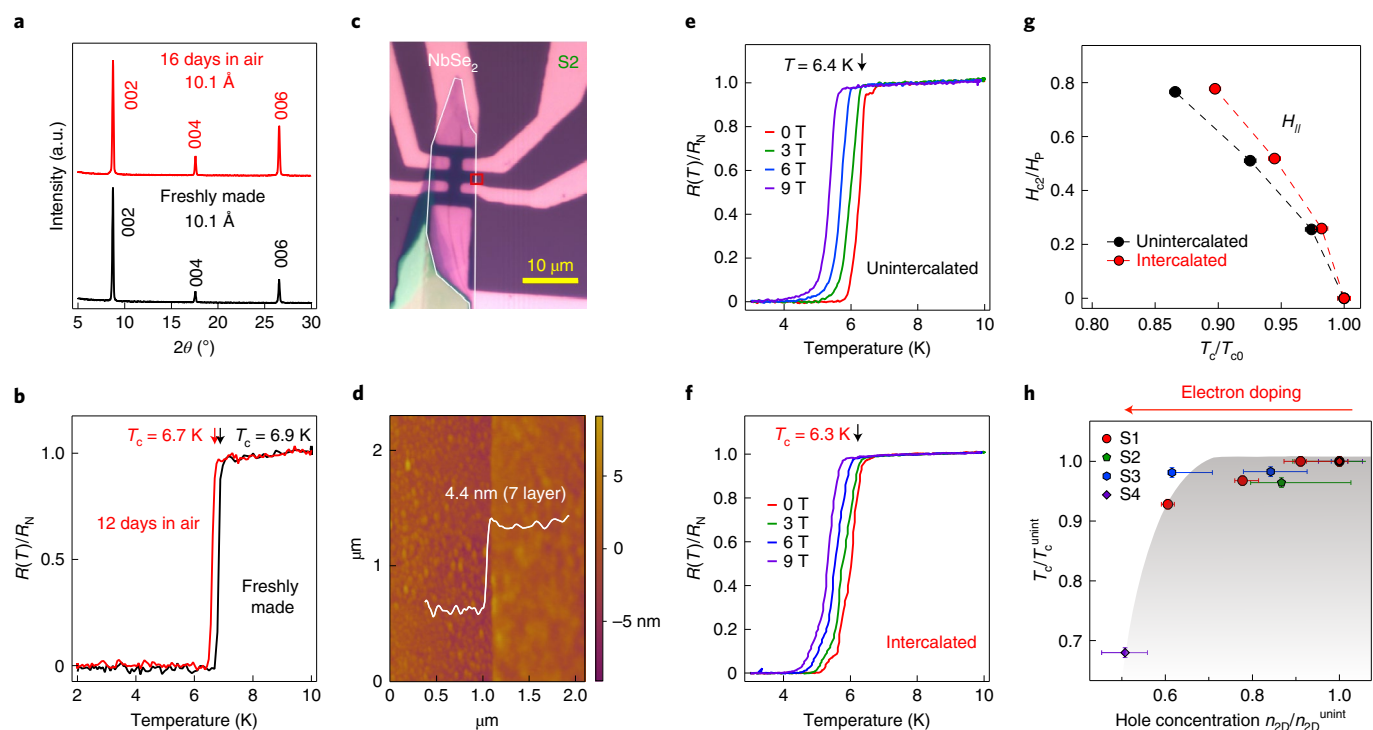
Fig. 4 | Sample stability and experimental results on intercalated few-layer flake samples. a, XRD data of [C$_2$MIm]$^+$-intercalated sample before and after storage under ambient conditions for 16 days. **b**, Resistance measurements of [C$_2$MIm]$^+$-intercalated sample before and after storage under ambient conditions for 12 days. **c,d**, Optical image (**c**) and AFM (**d**) of an exfoliated seven-layer NbSe$_2$ flake, which is indicated as S2 in **h**. The measured area is indicated by a red box in **c**. The height intensity is indicated by a linear colour scale, as indicated by the colour bar. The topographic line-profile (white curve) is obtained by integrating over the vertical direction of the image and shows a step height of 4.4 nm.

e,f, Resistance under different in-plane magnetic fields before (**e**) and after (**f**) [C$_2$MIm]$^+$ intercalation of this seven-layer flake sample. **g**, Extracted upper critical magnetic fields H_{c2} for $H_{\parallel}$ as a function of T_c before and after intercalation. **h**, T_c as a function of n_{2D} (extracted from Hall data measured at 75 K) for flake samples before and after intercalation. The thickness of these four flake samples is ten layers, seven layers, five layers and seven layers from S1 to S4, and they exhibit overall similar trend (see a comparison between red and purple symbols measured at different doping).

6.2 ± 0.1 Å disappear, and a new set of diffraction peaks with a larger interlayer spacing is clearly observed, indicating the effective intercalation of ions into the entire bulk crystal. To track which ions are intercalated, we compare three ILs with different cations and anions, respectively. The observation of similar interlayer spacing of 10.1 ± 0.1 Å for ILs containing the same cation (red and blue curves in Fig. 1c), and different interlayer spacings (10.1 ± 0.1 Å versus 19.7 ± 0.1 Å) for ILs containing the same anion but different cations (blue and green curves in Fig. 1c), provides definitive evidence that the cations from the ILs are intercalated. This is consistent with the negative polarity of the gating voltage, which drives positively charged cations into the sample. In addition, the absence of fluorine and sulfur peaks in the energy-dispersive X-ray spectroscopy (EDS) measurements using scanning electron microscopy (SEM) confirms that there is negligible intercalation of the anions from the ionic liquids (Supplementary Fig. 4). The successful cation intercalation leads to two distinct changes in the Raman spectra: the suppression of low-energy shear mode at 26.5 cm^{-1} and a blueshift of the E$_{2g}$ mode. The suppression of the shear mode is consistent with the reduced interlayer interaction similar to that observed in monolayer NbSe$_2$(ref. [16]), and the blueshift of the E$_{2g}$ mode similar to that observed in monolayer NbSe$_2$(ref. [16]) is attributed to reduced interlayer interaction or electron doping[27] from the intercalated cations.

Owing to the high quality of the organic–NbSe$_2$ hybrid crystal, ARPES measurements can be performed to reveal its corresponding electronic structure directly. Figure 2a,b shows a comparison of the electronic structures of a representative intercalated sample with a

[C$_2$MIm]$^+$ cation and unintercalated bulk NbSe$_2$. In both cases, the bands contributed by Nb 4d states[9,28,29] cross Fermi level (E_F), forming hole pockets at the Γ and K points (pointed by red and orange arrows in Fig. 2a and blue and green arrows in Fig. 3b). In sharp contrast, the highly dispersive 3D bands from the Se p_z state[28] at different k_z (out-of-plane momentum) values, which are observed in the unintercalated bulk sample as broad features (pointed by yellow arrow in Fig. 3b) due to the k_z broadening[30–32], are absent in the intercalated sample (see also second-derivative images in Supplementary Fig. 5), resulting in a large energy separation between the bottom of the conduction band and the top of the valence band (marked by yellow arrows in Fig. 2a). Such electronic structure is similar to that of monolayer NbSe$_2$(refs. [9,29]) and is also further supported by the first-principles calculations in Fig. 2c,d. The disappearance of the highly dispersive 3D Se p_z bands at the Γ point while maintaining the 2D Nb 4d bands shows that by expanding the interlayer spacing, the intercalated NbSe$_2$ exhibits effectively 2D electronic structure, although the intercalated sample is a bulk crystal.

To further reveal the difference between the intercalated sample and monolayer NbSe$_2$, we show in Fig. 2e–h a detailed comparison of the electronic structures of the intercalated sample and monolayer NbSe$_2$ film grown by molecular beam epitaxy (MBE)[13]. Although the dispersion is overall similar, there is a clear energy shift between these two samples. In particular, the bottom of the conduction band for the intercalated sample is shifted down by 0.14 eV, indicating that the intercalated sample is electron doped compared with the MBE film (see schematic drawings in the inset of Fig. 2g,h). Such electron doping is also confirmed by the Fermi surface maps, in which the intercalated

sample shows smaller hole pockets at both the Γ and K points (Fig. 2g). The 2D hole concentrations are calculated to be $7.5 \pm 0.1 \times 10^{14}$ cm^{-2} for the intercalated sample and $11.5 \pm 0.1 \times 10^{14}$ cm^{-2} for the MBE film from the size of the Fermi pockets based on the Luttinger theorem[33]. The smaller hole concentration confirms that there is electron doping for the intercalated sample. Therefore, the intercalation of cations not only provides an effective control for the interlayer interaction but also leads to substantial electron doping into the NbSe$_2$ layers.

To investigate the effect of the cation intercalation on the superconductivity, Fig. 3 shows a direct comparison of transport measurements before and after the intercalation. The intercalated sample shows an onset temperature $T_c^{onset} = 6.9$ K (defined as the 90% resistance of the normal state; Fig. 3a), which is comparable to $T_c^{onset} = 7.0$ K in the unintercalated bulk sample (Fig. 3b). Application of an out-of-plane magnetic field $H_\perp$ strongly suppresses the superconductivity for both samples (Fig. 3c,d); however, the suppression of superconductivity by in-plane magnetic field $H_\parallel$ is much less for the intercalated sample (Fig. 3e) compared with the unintercalated bulk sample (Fig. 3f). For example, high-field measurements show that superconductivity persists above 25 T for the intercalated sample (Fig. 3g). Figure 3h shows the extracted upper critical fields as a function of temperature. The extracted in-plane upper critical field $H_{c2,\parallel}^* = 41.9 \pm 1.2$ T is more than three times of the Pauli limit $H_P = 12.7$ T, where $H_P = 1.84\,T_{c0}$ (refs. [10,34,35]), where T_{c0} is the temperature where the sample enters zero-resistance state. Taking into account that the intercalated NbSe$_2$ consists of effectively decoupled NbSe$_2$ layers with spin–momentum locking similar to monolayer NbSe$_2$ (ref. [16]), the observation of large upper critical field exceeding the Pauli limit suggests that the intercalated sample exhibits Ising superconductivity similar to monolayer NbSe$_2$ (ref. [16]) and gated MoS$_2$ flake[23,24].

In addition to achieving a higher T_c than monolayer flake, the intercalated NbSe$_2$ sample also shows improved stability compared with monolayer NbSe$_2$. While monolayer NbSe$_2$ degrades within a few hours[10,11], the intercalated NbSe$_2$ sample is stable under ambient conditions for more than ten days both in terms of the crystal structure and superconducting properties, as is supported by XRD and transport measurements (Fig. 4a,b). The improved stability is in line with the intercalated black phosphorus[36] and intercalated MoTe$_2$ or WTe$_2$ (ref. [25]), where the intercalants protect the active 2D semiconducting/metallic monolayers and their properties such as superconductivity. In addition, further experiments on few-layer NbSe$_2$ flakes have shown that the intercalation method also works for few-layer flakes. Figure 4c shows the optical image of an exfoliated NbSe$_2$ flake, whose thickness is determined to be 4.4 nm (seven layers) by atomic force microscopy (AFM) measurements (Fig. 4d). The intercalated seven-layer NbSe$_2$ flake shows a $T_c = 6.3 \pm 0.1$ K (Fig. 4f), which is comparable to the bulk NbSe$_2$. While the change in T_c is negligible (from 6.4 ± 0.1 K to 6.3 ± 0.1 K) as shown in Fig. 4e,f, the intercalated seven-layer NbSe$_2$ flake shows an enhancement of the in-plane upper critical field (Fig. 4g). This shows that the intercalation method can also be extended to few-layer flakes to enhance the in-plane upper critical field without sacrificing the T_c substantially. To further reveal the effect of carrier concentration on the superconductivity, Fig. 4h shows a systematic investigation of T_c and carrier concentration for intercalated few-layer flake samples. While T_c remains almost the same for small electron doping, for high electron doping that corresponds to a smaller hole carrier concentration, T_c decreases substantially. Similar behaviour is also observed for bulk intercalated samples (Supplementary Fig. 6). This suggests that the electron doping from the intercalated cations is not critical for maintaining the high T_c in the intercalated sample and can be even suppressing T_c at high electron doping.

The tailored Ising superconductivity in the bulk intercalated NbSe$_2$ sample shows superconductivity with an onset temperature $T_c^{onset} = 6.9$ K, which is higher than the maximum $T_c^{onset} = 3.7$ K reported in monolayer flakes[4–8] and monolayer thin films[9–13] (see

Supplementary Table 2 for the summary). A comparison of our intercalated sample with monolayer flake provides some useful insights on the physics of monolayer NbSe$_2$. The intercalated NbSe$_2$ sample shows effectively 2D electronic structure similar to monolayer NbSe$_2$ yet without compromising the T_c, thereby suggesting that the absence of Se-derived bands[8,9] is unlikely the main reason for the suppression of T_c in monolayer NbSe$_2$. Instead, our work suggests that the depletion of the superconducting density of states near the monolayer superconductor–vacuum interface[8,37,38] and the competition between superconductivity and CDW are more likely reasons for the suppression of T_c in monolayer NbSe$_2$. In particular, our intercalated sample shows a lower CDW transition temperature $T_{CDW} \approx 68$ K (Supplementary Fig. 7) compared with monolayer sample, which shares a similar electronic structure with $T_{CDW} = 145$ K. The observation of a lower T_{CDW} and a higher T_c in the intercalated sample is in agreement with the competition between superconductivity and CDW[16–18] proposed in monolayer NbSe$_2$.

The interlayer interaction and carrier concentration have been two major controlling knobs for enriching the fundamental physics and intriguing properties of layered materials over the past two decades, and our work identifies intercalation of cations from ionic liquids as an effective route for simultaneous control of these two important parameters. The intercalation method is quite generic and can be readily extended to a large group of layered materials (for example, MoTe$_2$ and WTe$_2$(ref. [25]), TaSe$_2$, TaS$_2$, SnSe$_2$(ref. [26]), graphite and so on) with a wide variety of ILs with different cations (for example, [C$_n$MIm]$^+$ (1-alkyl-3-methyl-imidazolium, n represents the length of the alkane carbon chain), [DEMB]$^+$ (N,N-diethyl-N-butyl-N-methylammonium), [DEME]$^+$ (N,N-diethyl-N-(2-methoxyethyl)-N-methyl- ammonium) and [C$_n$MMIm]$^+$(1-alkyl-2,3-dimethyl-imidazolium, n represents the length of the alkane carbon chain); see Supplementary Figs. 8–10 and Supplementary Table 1). Therefore, our work provides an important methodology for creating hybrid materials with tunable functionalities possibly exceeding the bulk crystals and monolayer samples.

Online content

Any methods, additional references, Nature Research reporting summaries, source data, extended data, supplementary information, acknowledgements, peer review information, details of author contributions and competing interests, and statements of data and code availability are available at https://doi.org/10.1038/s41567-022-01778-7.

References

1. Wang, Q. H., Kalantar-Zadeh, K., Kis, A., Coleman, J. N. & Strano, M. S. Electronics and optoelectronics of two-dimensional transition metal dichalcogenides. *Nat. Nanotechnol.* **7**, 699–712 (2012).
2. Chhowalla, M. et al. The chemistry of two-dimensional layered transition metal dichalcogenide nanosheets. *Nat. Chem.* **5**, 263–275 (2013).
3. Manzeli, S., Ovchinnikov, D., Pasquier, D., Yazyev, O. V. & Kis, A. 2D transition metal dichalcogenides. *Nat. Rev. Mater.* **2**, 17033 (2017).
4. Xi, X. et al. Ising pairing in superconducting NbSe$_2$ atomic layers. *Nat. Phys.* **12**, 139–143 (2016).
5. Frindt, R. Superconductivity in ultrathin NbSe$_2$ layers. *Phys. Rev. Lett.* **28**, 299–301 (1972).
6. Staley, N. E. et al. Electric field effect on superconductivity in atomically thin flakes of NbSe$_2$. *Phys. Rev. B* **80**, 184505 (2009).
7. Cao, Y. et al. Quality heterostructures from two-dimensional crystals unstable in air by their assembly in inert atmosphere. *Nano Lett.* **15**, 4914–4921 (2015).
8. Khestanova, E. et al. Unusual suppression of the superconducting energy gap and critical temperature in atomically thin NbSe$_2$. *Nano Lett.* **18**, 2623–2629 (2018).

9. Ugeda, M. M. et al. Characterization of collective ground states in single-layer NbSe$_2$. *Nat. Phys.* **12**, 92–97 (2015).
10. Xing, Y. et al. Ising superconductivity and quantum phase transition in macro-size monolayer NbSe$_2$. *Nano Lett.* **17**, 6802–6807 (2017).
11. Wang, H. et al. High-quality monolayer superconductor NbSe$_2$ grown by chemical vapour deposition. *Nat. Commun.* **8**, 394 (2017).
12. Nakata, Y. et al. Anisotropic band splitting in monolayer NbSe$_2$: implications for superconductivity and charge density wave. *npj 2D Mater. Appl.* **2**, 12 (2018).
13. Zhao, K. et al. Disorder-induced multifractal superconductivity in monolayer niobium dichalcogenides. *Nat. Phys.* **15**, 904–910 (2019).
14. Yokoya, T. et al. Fermi surface sheet-dependent superconductivity in 2H-NbSe$_2$. *Science* **294**, 2518–2520 (2001).
15. Rahn, D. et al. Gaps and kinks in the electronic structure of the superconductor 2H-NbSe$_2$ from angle-resolved photoemission at 1 K. *Phys. Rev. B* **85**, 224532 (2012).
16. Xi, X. et al. Strongly enhanced charge-density-wave order in monolayer NbSe$_2$. *Nat. Nanotechnol.* **10**, 765–769 (2015).
17. Chu, C. W., Diatschenko, V., Huang, C. Y. & DiSalvo, F. J. Pressure effect on the charge-density-wave formation in 2H-NbSe$_2$ and correlation between structural instabilities and superconductivity in unstable solids. *Phys. Rev. B* **15**, 1340–1342 (1977).
18. Lian, C.-S., Chen, S. & Duan, W. Unveiling charge-density wave, superconductivity, and their competitive nature in two-dimensional NbSe$_2$. *Nano Lett.* **18**, 2924–2929 (2018).
19. Ueno, K. et al. Electric-field-induced superconductivity in an insulator. *Nat. Mater.* **7**, 855–858 (2008).
20. Ueno, K. et al. Discovery of superconductivity in KTaO$_3$ by electrostatic carrier doping. *Nat. Nanotechnol.* **6**, 408–412 (2011).
21. Ye, J. T. et al. Superconducting dome in a gate-tuned band insulator. *Science* **338**, 1193–1196 (2012).
22. Yamada, Y. et al. Electrically induced ferromagnetism at room temperature in cobalt-doped titanium dioxide. *Science* **332**, 1065–1067 (2011).
23. Saito, Y. et al. Superconductivity protected by spin-valley locking in ion-gated MoS$_2$. *Nat. Phys.* **12**, 144–149 (2016).
24. Lu, J. et al. Evidence for two-dimensional Ising superconductivity in gated MoS$_2$. *Science* **350**, 1353–1357 (2015).
25. Zhang, H. et al. Enhancement of superconductivity in organic-inorganic hybrid topological materials. *Sci. Bull.* **65**, 188–193 (2020).
26. Rousuli, A. et al. Induced anisotropic superconductivity in ionic liquid cation intercalated 1T-SnSe$_2$. *2D Mater.* **8**, 015024 (2020).
27. Das, A. et al. Monitoring dopants by Raman scattering in an electrochemically top-gated graphene transistor. *Nat. Nanotechnol.* **3**, 210–215 (2008).
28. Johannes, M., Mazin, I. & Howells, C. Fermi-surface nesting and the origin of the charge-density wave in NbSe$_2$. *Phys. Rev. B* **73**, 205102 (2006).
29. Calandra, M., Mazin, I. I. & Mauri, F. Effect of dimensionality on the charge-density wave in few-layer 2H-NbSe$_2$. *Phys. Rev. B* **80**, 308–310 (2009).
30. Sobota, J. A., He, Y. & Shen, Z.-X. Angle-resolved photoemission studies of quantum materials. *Rev. Mod. Phys.* **93**, 025006 (2021).
31. Kirchner, S. et al. Colloquium: Heavy-electron quantum criticality and single-particle spectroscopy. *Rev. Mod. Phys.* **92**, 011002 (2020).
32. Zhang, H. et al. Angle-resolved photoemission spectroscopy. *Nat. Rev. Methods Primers* **2**, 54 (2022).
33. Luttinger, J. Fermi surface and some simple equilibrium properties of a system of interacting fermions. *Phys. Rev.* **119**, 1153–1163 (1960).
34. Chandrasekhar, B. A note on the maximum critical field of high-field superconductors. *Appl. Phys. Lett.* **1**, 7–8 (1962).
35. Clogston, A. M. Upper limit for the critical field in hard superconductors. *Phys. Rev. Lett.* **9**, 266–267 (1962).
36. Wang, C. et al. Monolayer atomic crystal molecular superlattices. *Nature* **555**, 231–236 (2018).
37. Simonin, J. Surface term in the superconductive Ginzburg–Landau free energy: application to thin films. *Phys. Rev. B* **33**, 7830–7832 (1986).
38. de Gennes, P. G. *Superconductivity of Metals and Alloys* (Benjamin, New York, 1966).

Methods

Sample growth

High-quality $NbSe_2$ single crystals were synthesized by the I_2 chemical vapour transport method. Polycrystalline $NbSe_2$ were synthesized by heating the high-purity stoichiometric mixture of Nb powder (99.99%, Alfa Aesar) and Se ingot (99.99%, Alfa Aesar) at 800 °C in a vacuum-sealed silica ampoule for several days. Using a chemical vapour transport method with I_2 as transfer agent, polycrystalline $NbSe_2$ were transferred from a high-temperature (820 °C) area to a low-temperature (750 °C) area to achieve recrystallization. High-quality $NbSe_2$ single crystals were obtained after several days. Monolayer $NbSe_2$ film was grown under a Se-rich condition and monitored by in situ reflection high-energy electron diffraction[13].

Bulk sample intercalation

The intercalation of ionic liquid cations is achieved through electrochemical reaction with a simple lab-design intercalation device as shown in Fig. 1b. High-quality $NbSe_2$ single-crystal sample acts as the working electrode, which is immersed in the ionic liquid electrolyte, and Pt is used as the counter electrode. Applying a negative voltage with the electrochemical workstation can drive organic cations into $NbSe_2$ layers. And an appropriate heating temperature could remarkably increase the intercalation efficiency. A globally intercalated bulk with typical thickness of 100 μm can be obtained within a few hours.

X-ray diffraction

The XRD patterns are collected from a diffractometer using Cu K_α ($\lambda = 1.5418$ Å) radiation to reveal the interlayer spacings of the samples. The samples are mounted in reflection geometry with the Q-vector (scattering vector) along the out-of-plane direction.

ARPES measurements

ARPES measurements were performed in our home laboratory at Tsinghua with a helium discharge lamp. The samples were oriented by Laue before loaded into the ARPES chamber, and the freshly cleaved surface was measured at 80 K under an ultrahigh vacuum better than 1×10^{-10} torr. The data were recorded by a Scienta DA30-L with a photon energy of 21.2 eV.

Device fabrication

Few-layer $NbSe_2$ flakes are fabricated in a glovebox (H_2O <0.1 ppm, O_2 <0.1 ppm) from unintercalated single crystal on polydimethylsiloxane stamps and transferred to pre-patterned Ti/Au (5 nm/30 nm) Hall bar on Si/SiO_2 substrate. Hexagonal boron nitride thin flakes are fabricated and transferred in the same strategy. The thickness of $NbSe_2$ and hexagonal boron nitride flakes are confirmed by AFM measurements.

Transport measurements

Transport measurements were performed in a Physical Property Measurement System (PPMS, Quantum Design) with the lowest temperature of 1.6 K and magnetic field up to 9 T. The longitudinal resistances were measured through a four-probe method, and a small excitation current (50 μA) was employed to avoid sample heating. The high-magnetic-field transport measurements were performed on the Steady High Magnetic Field Facilities, High Magnetic Field Laboratory, CAS.

Theoretical calculation

First-principles calculations were performed in the framework of density functional theory as implemented in the Vienna ab initio Simulation Package (VASP)[39]. The projector augmented wave method and the Perdew–Burke–Ernzerhof-type exchange correlation functional[40] and the plane-wave basis with an energy cut-off of 400 eV were used. Van der Waals corrections were included by the zero damping DFT-D3 method[41]. The spin–orbit coupling was included in self-consistent electronic structure calculations. A $16 \times 16 \times 14$ k-point mesh grid was taken for bulk calculations. The atomic structure was fully relaxed with a force criterion of 0.001 eV Å^{-1}.

Data availability

Source data are available with this paper. Other data that support the findings of this study are available from the corresponding author upon reasonable request.

References

39. Kresse, G. & Furthmüller, J. Efficiency of ab-initio total energy calculations for metals and semiconductors using a plane-wave basis set. *Comput. Mater. Sci.* **6**, 15–50 (2019).
40. Perdew, J. P., Burke, K. & Ernzerhof, M. Generalized gradient approximation made simple. *Phys. Rev. Lett.* **77**, 3865–3868 (1996).
41. Grimme, S., Antony, J., Ehrlich, S. & Krieg, H. A consistent and accurate ab initio parametrization of density functional dispersion correction (DFT-D) for the 94 elements H–Pu. *J. Phys. Chem. Lett.* **132**, 154104 (2010).

Acknowledgements

Author contributions

S.Z. and P.Y. conceived the research project. Haoxiong Zhang, A.R., C.G., L.L., R.F. and Y.W. grew, intercalated and characterized the samples. A.R., Haoxiong Zhang, Kenan Zhang, C.B., Hongyun Zhang and W.Y. performed the ARPES measurements and analysed the ARPES data. Haoxiong Zhang, S.S. and P.Y. performed the transport measurements. Kun Zhao., S.J., Xi Chen and Q.-K.X. grew the monolayer $NbSe_2$ MBE film for ARPES measurements. Haoxiong Zhang, Xin Cong and P.T. performed the Raman measurements and analysed the Raman data. Z.L., S.X., Y.X. and W.D. performed the first-principles calculations. Haoxiong Zhang, P.Y. and S.Z. wrote the manuscript, and all authors commented on the manuscript.

Competing interests

The authors declare no competing interests.

Additional information

Supplementary information The online version contains supplementary material available at https://doi.org/10.1038/s41567-022-01778-7.

Correspondence and requests for materials should be addressed to Shuyun Zhou.

Peer review information *Nature Physics* thanks the anonymous reviewers for their contribution to the peer review of this work.

Reprints and permissions information is available at www.nature.com/reprints.